Femtosecond pulse propagation in argon: A pressure dependence study

M. Mlejnek,* E. M. Wright, and J. V. Moloney

Arizona Center for Mathematical Sciences, University of Arizona, Tucson, Arizona 85721
and Optical Sciences Center, University of Arizona, Tucson, Arizona 85721

We present a numerical study of self-focusing and optical breakdown of focused femtosecond pulses in argon using an extended nonlinear Schrödinger equation for the field coupled to an equation for the electron density generated via multiphoton ionization. Using the pressure as a control parameter we are able to identify different regimes of femtosecond pulse propagation from a low-pressure regime dominated by plasma effects ($p \lesssim 1$ atm) to full blown self-focusing collapse arrested by normal group velocity dispersion at high pressures ($p \gtrsim 100$ atm). In the intermediate region ($p \sim 1-10$ atm) the dynamics of the pulse propagation is affected by both self-focusing and plasma effects and can lead to multiple collapse events and also stabilized propagation. [S1063-651X(98)13509-2]

I. INTRODUCTION

There has been considerable interest in nonlinear pulse propagation in the transparency region of atomic and molecular gases over the past decade. Experiments have been performed for a number of gases and a large range of pressures showing different characteristic effects. In the low-pressure or collisionless regime ($p \ll 1$ atm) multiphoton ionization (MPI) [1–3] and plasma-induced blueshifting of femtosecond pulses have been studied [4–8], along with plasma-induced spatial defocusing [9,10] and a light pipe for laser pulses [11]. In contrast, for higher pressures ($p > 1$ atm), in the collisional regime, nonlinear optical self-focusing (SF) becomes important when the peak input power exceeds the critical power for self-focusing [12–14] leading to supercontinuum generation and optical breakdown [15–18].

In this paper we present a numerical study of femtosecond pulse propagation in argon using the pressure as a control parameter, our goal being to identify and elucidate the different regimes of nonlinear pulse propagation. We have chosen Ar as a representative example of pulse propagation in the noble gases and also because detailed parameters are available for the linear and nonlinear optical properties. Our motivation for undertaking this study was to investigate the relative roles of SF, MPI, plasma-induced effects, and group velocity dispersion (GVD) for femtosecond pulse propagation in the transparency region of gases. In particular, for peak input powers exceeding the critical power for SF the paraxial wave theory of SF predicts beam collapse to a singularity in a finite distance [12–14], but this clearly cannot happen physically. This raises the issue of what physical mechanisms intervene to arrest, or regularize, the SF collapse. For example, as the collapse proceeds the concomitant high intensities can lead to MPI and optical breakdown,

thereby reducing the power below the critical power and arresting the collapse. In this process spatial defocusing due to the generated electron plasma can also halt the collapse. In other work Strickland and Corkum suggested [19,20] and others [21–26] have shown that normal GVD can arrest self-focusing collapse by causing the incident pulse to split into two pulses of reduced peak power. Our goal in this paper is to establish which collapse regularizing mechanisms are operative in which pressure regimes and to identify the characteristic propagation phenomena in each regime. Since we are primarily concerned with beam collapse and the critical power scales as the inverse pressure, we shall concentrate on pressures $p > 1$ atm.

The remainder of this paper is organized as follows. In Sec. II we describe our theoretical model for pulse propagation in Ar, along with the material parameters and their variation with pressure. Section III describes our computer simulations in the various pressure regimes and elucidates the characteristic phenomena in each. A discussion of the results is given in Sec. IV and our summary and conclusions are given in Sec. V.

II. THEORETICAL MODEL

In this section we describe our theoretical model for pulse propagation in Ar, in which an extended nonlinear Schrödinger equation (NLSE) for the electric field envelope is coupled to an equation for the electron density generated via MPI. This model is a nonlinear extension of one employed by Feit and Fleck [27] to study plasma defocusing effects and has previously been successfully used by Feng *et al.* to study nonlinear pulse propagation in water [28].

A. Model equations

Assuming propagation along the z axis and that the field remains cylindrically symmetric, the equation for the electric field envelope $\mathcal{E}(r,z,t)$ in a reference frame moving at the group velocity is [28]

*Also at Physics Department, University of Ostrava, Bráfova 7, Ostrava, Czech Republic.

$$\frac{\partial \mathcal{E}}{\partial z} = \frac{i}{2k}\left(\frac{\partial^2}{\partial r^2} + \frac{1}{r}\frac{\partial}{\partial r}\right)\mathcal{E} - \frac{ik''}{2}\frac{\partial^2 \mathcal{E}}{\partial t^2} + ik_0 n_2 |\mathcal{E}|^2 \mathcal{E}$$

$$-\frac{\sigma}{2}(1 + i\omega\tau)\rho\mathcal{E} - \sum_K \frac{\beta^{(K)}}{2}|\mathcal{E}|^{2K-2}\mathcal{E}, \qquad (1)$$

where the terms on the right-hand side describe transverse beam diffraction, GVD, nonlinear SF, absorption and defocusing due to the electron density ρ, and MPI processes involving K photons. Here ω is the optical frequency, $|\mathcal{E}|^2$ is the intensity, $k = n_b k_0 = n_b \omega/c$, the quantity $k'' = \partial^2 k/\partial\omega^2$ controls the magnitude and sign of the GVD, with $k'' > 0$ corresponding to normal dispersion and $k'' < 0$ to anomalous dispersion, $n_2 > 0$ is the nonlinear coefficient such that the nonlinear change in the refractive index is $n_2|\mathcal{E}|^2$, σ is the cross section for electron-neutral inverse bremsstrahlung, τ is the electron collision relaxation time, and $\beta^{(K)}$ is the nonlinear coefficient for K-photon absorption. The order of the MPI is obtained from $K = \lceil(U_i/\hbar\omega)\rceil$, which is the minimum number of photons of energy $\hbar\omega$ needed to overcome the ionization energy U_i for liberating an electron. In general we allow for different orders of MPI to be present, each with a different value of K, but for the numerical simulations presented here we specialize to one order.

The propagation Eq. (1) is an extended NLSE that accounts for the combined effects of linear GVD, SF, and nonlinear absorption and defocusing due to the electron plasma. In deriving this equation several approximations have been made: In addition to the usual slowly varying envelope approximations in space and time we retain only second-order GVD as characterized by k'', we treat both the nonlinear refractive index (n_2) and nonlinear absorption ($\beta^{(K)}$) as local in time, and we assume that the optical properties of the generated electron plasma (term proportional to σ) may be calculated quasistatically. The restriction to second-order GVD is not an essential approximation and may be relaxed, but we retain this description since recent work has shown that second-order normal dispersion may already halt self-focusing collapse [19–26] and our prime concern here is to show how the various physical effects regularize collapse in different pressure regimes. We have treated the nonlinear refractive-index change as local in time based on the assumed nonresonant light-matter interaction and similarly for the MPI where we assume no resonant enhancement. Finally, we may treat the optical response of the plasma quasistatically if the pulse duration t_p is greater than the electron-atom collision time τ, so that the plasma always remains close to equilibrium (we also neglect any frequency energy dependence of the scattering rates). For a pressure of 10 atm, which is in the midrange of what we will consider, the electron-atom collision time is $\tau \approx 10$ fs, which is much less than the 200-fs pulses we consider here.

To describe the generation of electrons by the process of MPI in Ar we employ the results of Ref. [3]. These authors considered both the lowest-order perturbation theory of MPI and the tunneling ionization theory and compared the results with experiments on the yield of multiply charged ions. The perturbation theory expression for MPI coincides with the general Keldysh theory [29] in the limit of $\gamma \gg 1$, where $\gamma^2 = U_i/2U_q$, with $U_q = e^2 \mathcal{E}^2/4m_e\omega^2$ the quiver energy. In the
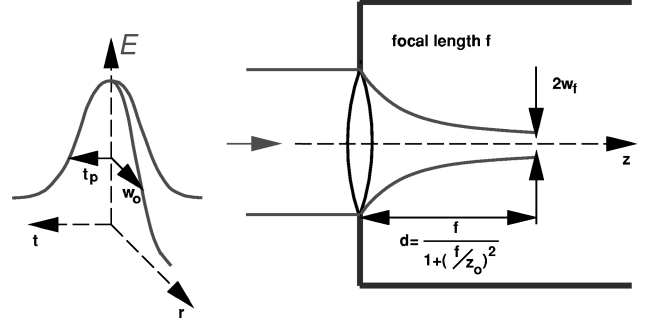

FIG. 1. Propagation geometry considered in the text. The pulse is incident onto the variable pressure gas cell through a thin lens of focal length f.

opposite regime $\gamma \ll 1$ the tunneling theory applies. For the present study with peak intensities $I_p \lesssim 10^{14}$ W/cm^2, we find $\gamma \sim 1$, so that neither extreme applies. However, Perry *et al.* [3] found that the functional form of the perturbation theory result applies well even in this regime as long as an effective value for the MPI coefficient $\beta^{(K)}$ is employed, which is obtained from the experiment. This is the approach we adopt in the present paper. Then the rate of generation of the electron density due to MPI is given by

$$\left(\frac{\partial \rho}{\partial t}\right)_{MPI} = \frac{\beta^{(K)}|\mathcal{E}|^{2K}}{K\hbar\omega}. \qquad (2)$$

In using this simplified model we assume that only singly charged ions are produced, which is consistent with the restriction to intensities $I_p \lesssim 10^{14}$ W/cm^2, and that the electron density remains much less than the atomic density $\rho \ll N_a$. We are also ignoring some of the finer details of MPI including above-threshold ionization [30] and the frequency dependence of the MPI cross section.

To complete our model for the electron plasma we also allow for cascade ionization and radiative recombination, which yields the final equation [27,31]

$$\frac{\partial \rho}{\partial t} = \frac{1}{n_b^2}\frac{\sigma}{U_i}\rho|\mathcal{E}|^2 + \frac{\beta^{(K)}|\mathcal{E}|^{2K}}{K\hbar\omega} - \alpha\rho^2. \qquad (3)$$

The first term on the right-hand side of this equation describes the growth of the electron plasma by cascade (avalanche) ionization, the second term is the contribution of MPI, which acts both as a source for the cascade process and as a contributor to plasma growth, and the third term describes the radiative electron recombination. For the subpicosecond pulses considered here cascade ionization is not expected to play a major role, but we include it for completeness. In addition, if there is a free electron density in the Ar prior to the pulse it will also be amplified by cascade ionization. Thus we also include a background initial density ρ_b as an initial condition.

B. Focusing geometry and material parameters

Figure 1 shows the focusing geometry considered here. We are interested in the situation where an initial collimated Gaussian beam enters the Ar sample following a lens of focal length f,

$$\mathcal{E}(r,0,t) = \sqrt{\frac{2P_{in}}{\pi w_0^2}} \exp\left[-\frac{r^2}{w_0^2}\left(1 + \frac{ikw_0^2}{2f} \right) - \frac{t^2}{t_p^2} \right], \quad (4)$$

where P_{in} is the peak input power $[P(t) = \int 2\pi r dr |\mathcal{E}(r, z=0,t)|^2 = P_{in}\exp(-2t^2/t_p^2)]$, w_0 is the spot size, and $\tau_p = 2t_p$ is the full temporal width at the $1/e^2$ points of the pulse intensity distribution. In what follows we shall quote the values of the full width at half maximum of irradiance, which is $\tau_{FWHM} = \sqrt{2 \ln 2} \tau_p$, since it is the more generally accessible experimental quantity. Under conditions of linear focusing the input Gaussian beam comes to a focus at a longitudinal position $d = f/(1 + f^2/z_0^2)$, where $z_0 = \pi w_0^2 n_b/\lambda_0$ is the Rayleigh range (diffraction length) of the input beam. The size of the laser beam w_f at the focus is $(w_f/w_0)^2 = (f^2/z_0^2)/(1 + f^2/z_0^2) = z_f/z_0$, with z_f the Rayleigh range of the focused beam.

For the numerical simulations to be presented here we consider the characteristic visible wavelength of $\lambda_0 = 586$ nm, for which the parameters appropriate to Ar at a pressure $\tilde{p}$ measured in atmospheres are $n_b = 1.0 + 2.7 \times 10^{-4}\tilde{p}$ from the Sellmeier formula in [32], $n_2 = 4.9 \times 10^{-19}\tilde{p}$ cm^2/W calculated using the approach of [33] for the Ar data in [34,35], $K = 8$, $\beta^{(8)} = 3.5 \times 10^{-123}\tilde{p}$ m^{13} W^{-7} [36], $U_i = 15.76$ eV, and $\tau = \tau_0/\tilde{p}$, where $\tau_0 = 1.9 \times 10^{-13}$ s [37]. The cross section for electron-neutral inverse bremsstrahlung may be calculated using $\sigma = (ke^2/\omega m \epsilon_0)\{\tau/[1 + (\omega\tau)^2]\}$, giving $\sigma \simeq (5.46 \times 10^{-24} n_b$ m$^2/\tilde{p})[1 + (\omega\tau_0)^2]/[1 + (\omega\tau_0/\tilde{p})^2]$. Figure 2 shows the variation of the various material parameters with pressure. The coefficient of radiative electron recombination α is assumed to be pressure independent and we adopted the value of 7×10^{-13} m^{-3}/s for it.

The GVD for Ar was obtained using the Sellmeier formula for the refractive index $n(\omega)$ given by [32] from which $k(\omega) = \omega n(\omega)/c$ was formed and the GVD calculated. At the wavelength of 586 nm this yields normal GVD with a value $k'' = 0.26\tilde{p}$ fs^2/cm. The critical power for SF collapse in the absence of plasma generation is calculated using $P_{cr} = \lambda_0^2/2\pi n_b n_2$, which yields the pressure dependent critical power $P_{cr}(\tilde{p}) \simeq (1.12$ GW$)/n_b\tilde{p}$ for the above parameters.

We have performed extensive numerical simulations of propagation in Ar for a wide range of pressures and input field conditions. For the numerical simulations presented here the parameters of the input field were chosen as $\tau_{FWHM} = 200$ fs, $f = 2.5$ cm, and $w_0 = 200$ μm, giving a Rayleigh range of $z_0 = 21$ cm. We have chosen a focused input field for two reasons. First, for a collimated input beam the peak intensity decreases with distance unless SF takes place, thereby linking MPI with SF, unless the input intensity exceeds the threshold for MPI. By introducing linear focusing we also allow for the case where MPI can occur without associated SF and this allows us to study the transitions from SF dominated propagation to plasma and MPI dominated propagation. Second, by introducing linear focusing the propagation distances required to see the characteristic pulse propagation effects are more realistic in terms of computation time.
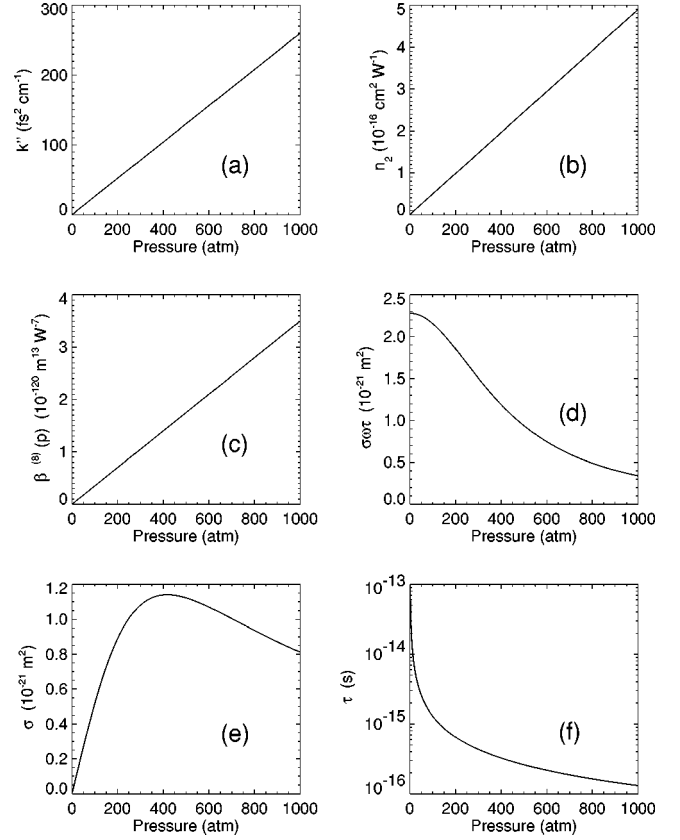

FIG. 2. Pressure dependence of the material parameters for Ar: (a) k'' governing GVD, (b) the SF coefficient n_2, (c) the MPI coefficient $\beta^{(8)}$, (d) $\sigma\omega\tau$, which governs plasma-induced self-phase modulation, (e) the cross section σ, which governs plasma absorption, and (f) the electron collision time τ.

C. Pressure-dependent regimes

As a precursor to the numerical simulations to be presented in Sec. III we first discuss the relative magnitudes of the effects appearing in the extended NLSE (1) as the pressure is varied. Referring to Fig. 2 we see that (a) the GVD (k''), (b) SF (n_2), and (c) MPI ($\beta^{(8)}$) all increase linearly with pressure, as expected physically since the density is increasing at fixed temperature and these effects therefore dominate at high pressures.

This is the high-pressure regime for $p \gtrsim 1000$ atm. In contrast, at low pressures the critical power for SF diverges and SF ceases to be important, and similarly for the GVD, but plasma-induced self-phase modulation and defocusing that is controlled by the product $\sigma\omega\tau$ in Fig. 2(d) becomes large and dominates [15]. We remark that the parameter σ in Fig. 2(e), which controls plasma absorption, actually decreases at low pressure, but the self-phase modulation survives since it also involves the electron collision rate τ in Fig. 2(f), which increases with decreasing pressure (density). This is the low-pressure collisionless regime $p \lesssim 1$ atm. For intermediate pressures all the effects are present and SF, MPI, and optical breakdown all participate in the dynamics.

Figure 3 shows the characteristic regimes of behavior for Ar gas based on the computational results that are described in the next section. In the high-pressure regime we observe strong self-focusing that is arrested by normal GVD and/or MPI [38], whereas the low-pressure regime is dominated by
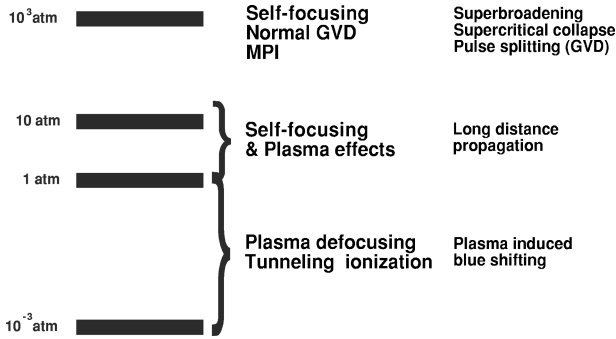
FIG. 3. Interesting pressure regimes identified for propagation in Ar, along with the operative physical mechanisms and the characteristic propagation phenomena.

plasma blueshifting and defocusing with little influence from SF: For this reason we do not dwell much on this regime. There is also an interesting transition regime for intermediate pressures $1 < p < 10$ atm where the SF and plasma effects become comparable and produce interesting propagation effects. We now turn to the detailed numerical simulations and present representative examples of the characteristic pulse propagation effects in each pressure regime.

III. NUMERICAL SIMULATIONS

Equations (1) and (3) with the inital conditions (4) and $\rho_b \approx 10^9$ cm^{-3} (rather pure gas) were solved using the split-step method of the Strang type in which the propagation is broken into small consecutive linear and nonlinear steps [39]. In the linear steps we advance the transverse Laplacian using finite differences (Crank-Nicholson scheme with transparent boundary conditions [40]) and also calculate the linear dispersion part (spectrally) of the field equation. The plasma equation is solved (using the Crank-Nicholson scheme) during the nonlinear field step (using the Runge-Kutta scheme), which includes the Kerr part of the nonlinearity. The typical grid sizes were $2.5w_0$ in the radial direction and $5\tau_{FWHM}$ in the time domain and the Δz step was chosen to ensure that the phase difference between two adjacent points be small compared to π.

A. High-pressure regime

In the high-pressure regime SF, GVD, and MPI are the operative physical mechanisms, though we retain all effects in our numerical simulations. The critical power for SF in the high-pressure regime $p \sim 1000$ atm is $P_{cr} \sim 1$ MW, with corresponding peak intensity $I_p \sim 10^9$ W/cm^2 for a spot size of $w_0 = 200$ μm. The peak input intensity is therefore well below the ionization thresholds $I_{th} \sim 10^{13} - 10^{14}$ W/cm^2 to generate electron densities of the order $\rho_{th} \approx 10^{17} - 10^{18}$ cm^{-3}, which are capable of absorbing the field and arresting SF collapse. Therefore, for peak powers exceeding the critical power the collapse can proceed a considerable distance before the effects of MPI become important, in which case the envelope approximations underlying our model may be violated. However, it was shown in Refs. [21–24] that normal GVD can arrest collapse through a pulse splitting process before the envelope approximations are violated. In this process self-modulation produces a positive fre-
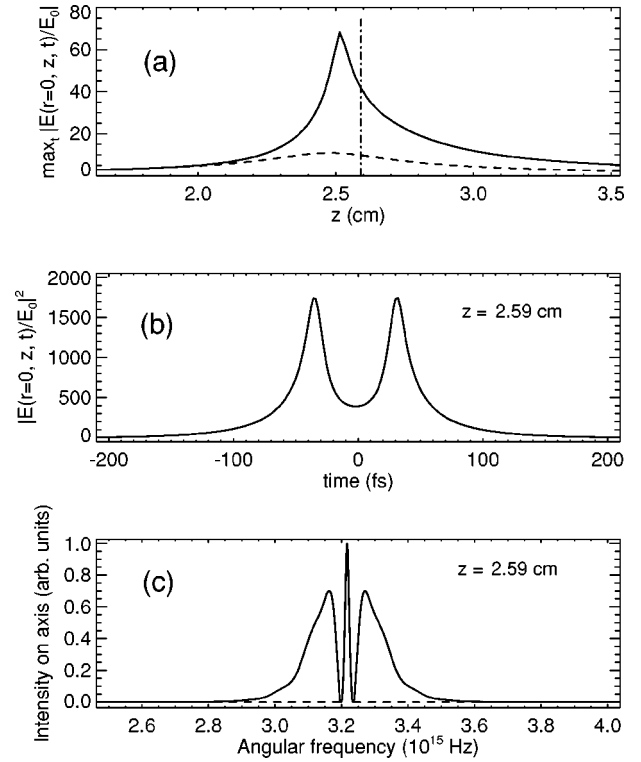

FIG. 4. (a) Maximum on-axis field amplitude over time showing the initial SF collapse and its arrest for $p = 1000$ atm and $P = 0.94P_{cr}$, (b) on-axis intensity as a function of time at the propagation distance $z = 2.59$ cm, and (c) the corresponding superbroadened normalized spectral intensity. The dash-dotted line in (a) shows the z position at which the field characteristics of (b) and (c) are shown. [The dashed line in (a) denotes the behavior of the maximum on-axis field amplitude over time for linear Gaussian beams.]

quency chirp across the pulse and normal GVD then pulls apart the two oppositely frequency-shifted halves of the pulse, thereby reducing the peak power and arresting the collapse.

An example of the pulse-splitting phenomenon for Ar at $p = 1000$ atm is shown in Fig. 4 for $P_{in} = 0.94P_{cr}$, just below the critical power but close enough to cause considerable nonlinear focusing especially in combination with the linear focusing: For higher input powers above the critical value pulse splitting is still observed in our numerics though the collapse is no longer arrested by normal GVD as in the example shown, that is, our numerical scheme breaks down. For the pressure $p = 1000$ atm used above the normal GVD of Ar is comparable to condensed matter systems, e.g., water and fused silica, and multiple pulse splitting without associated MPI has been reported for experiments in fused silica [25].

Figure 4(a) shows the maximum on-axis intensity over time as a function of propagation distance and the initial SF collapse, which is arrested at $z \approx 2.51$ cm, after which the intensity decreases monotonically. The on-axis pulse profile at $z = 2.59$ cm, just past the linear focus, is shown in Fig. 4(b) and shows the pulse-splitting effect. The corresponding superbroadened spectrum is shown in Fig. 4(c) and we see that it remains highly symmetric: This is direct evidence that the asymmetric spectral effects of plasma-induced blueshifting are not present in the high-pressure regime. In Fig. 5 we
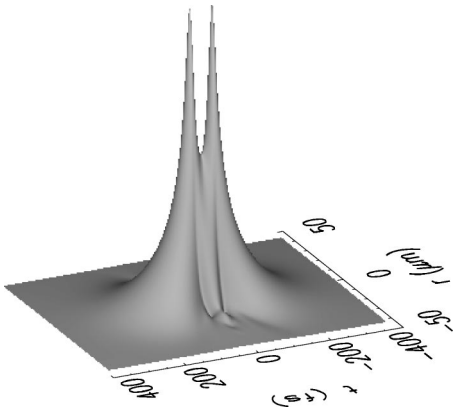
FIG. 5. Space-time (r,t) pulse profile at the propagation distance $z=2.59$ cm, $p=1000$ atm, and $P_{in}=0.94P_{cr}$.

show the full spatio-temporal profile of the pulse at $z = 2.59$ cm and considerable pulse reshaping is evident.

Figures 4 and 5 are representative of our findings in the high-pressure regime: SF collapse arrested by normal GVD with little influence from MPI or plasma effects. However, as the pressure is reduced below $p=1000$ atm the normal GVD is reduced in size and is no longer as effective at arresting the collapse. For example, for $p=100$ atm we found that neither normal GVD or MPI could arrest the SF collapse in our model before the envelope approximations were violated in space and time. This clearly calls for higher-order corrections to the envelope approximations [41–43], which is beyond the scope of the present paper or, more generally, for transitioning from the envelope description to a numerical solution based on the full Maxwell equations in the vicinity of the collapse. What we would like to draw attention to is the fact that there exists a pressure range for propagation in Ar for which the envelope description becomes invalid under propagation and this provides an experimental testing ground for propagation theories beyond the usual slowly varying approximations in space and time.

B. Low-pressure regime

In the low-pressure regime plasma-induced defocusing dominates over the effects of SF and GVD. Indeed, such a situation occurs for our parameters and geometry in Ar already at a pressure of $p=1$ atm: For an input power equal to the critical power $P_{cr} \sim 1.12$ GW the peak input intensity is of the order of the ionization intensity, thus precluding any strong SF effects. In Fig. 6(a) the on-axis electric field maximum (over time) is plotted as a function of the propagation distance z. We can see that the initial collapse is soon stopped by the defocusing caused by the generated plasma. The corresponding on-axis density profile versus z is shown in Fig. 6(b) and shows the strong plasma generation as the self-focusing is arrested.

The on-axis field as a function of time at a distance of 2.3 cm (after the nonlinear focus but still before the linear focus prediction) is shown in Fig. 7(a). After the collapse is stopped by the plasma generated by the front part of the pulse, the trailing edge of the pulse interacts with the generated plasma and is defocused, causing a time shift of the on-axis pulse to earlier times (in the moving reference frame). We can get a better picture of the pulse shape after
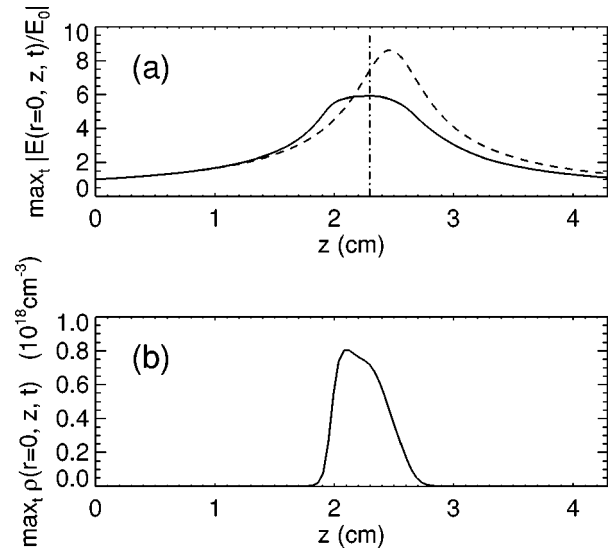

FIG. 6. (a) Maximum over time of the on-axis electric field amplitude and (b) on-axis density of generated plasma for $p = 1$ atm and $P_{in}=P_{cr}$. The dash-dotted line in (a) shows the z position at which the the field characteristics in Fig. 7 are shown. [The dashed line in (a) denotes the behavior of the maximum on-axis field amplitude over time for linear propagation.]

the onset of the plasma effect from Fig. 8, which shows the space-time pulse profile at $z=2.3$ cm: Here we clearly see that the trailing edge of the pulse is defocused into rings. There are also marked temporal asymmetries associated with the plasma generation process as shown in Fig. 8. These asymmetries are also present in the pulse spectrum, which shows a plasma-induced blueshift; see Fig. 7(b) [4,44,45]. We did not investigate the regime of lower Ar pressures $p<1$ atm in much detail because for our parameters in this region the plasma generation is so strong that the observed effect of nonlinear self-focusing is still smaller and our model becomes an approximation to the models describing
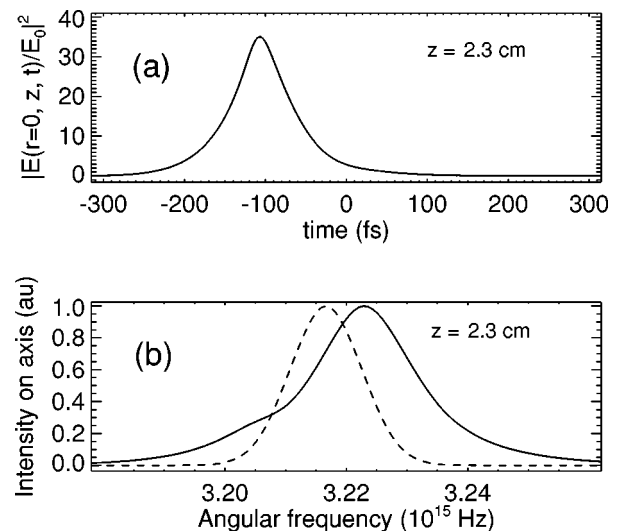

FIG. 7. (a) On-axis intensity as a function of time at the propagation distance $z=2.3$ cm and (b) the corresponding normalized spectral intensity for $p=1$ atm and $P_{in}=P_{cr}$. [The dashed line in (b) denotes the initial $(z=0$ cm) normalized spectral intensity.]
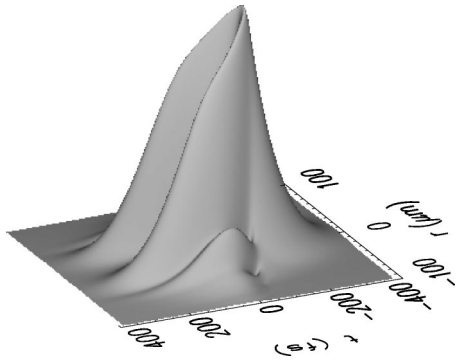
FIG. 8. Space-time (r,t) pulse profile at the propagation distance $z=2.3$ cm, $p=1$ atm, and $P_{in}=P_{cr}$.

multiple ionization by intense laser fields at lower pressures via tunneling ionization [6–8,10].

C. Transition region: Supercontinuum generation

There is a region of pressures where both Kerr nonlinearity and plasma effects are of the same magnitude resulting in competition between SF and plasma defocusing. Figures 9–11 show a series of space-time (r,t) plots for the pulse profile (upper plot) and corresponding electron density (lower plot) for different propagation distances z, for $p=10$ atm and $P_{in}=1.975P_{cr}$, with $P_{cr}\sim 0.1$ GW. These figures show that after the initial focusing (linear and nonlinear) the growth of the field amplitude (therefore the intensity) is arrested, with a concomitant increase in the electron density. Thus, in this case the SF collapse is arrested by MPI. However, as seen in Figs. 10–11, as the pulse propagates it develops temporal structure, in particular a double-peaked structure. This second pulse develops on the trailing edge of the pulse as the leading pulse decays due to MPI absorption. Physically, as the initial pulse self-focuses the leading edge generates plasma, which serves to defocus the trailing edge into spatial rings; see Fig. 10. However, with increasing propagation distance and as the leading edge pulse decays, the spatial rings reform under the action of self-focusing and produce the trailing edge pulse (see Fig. 11). We previously
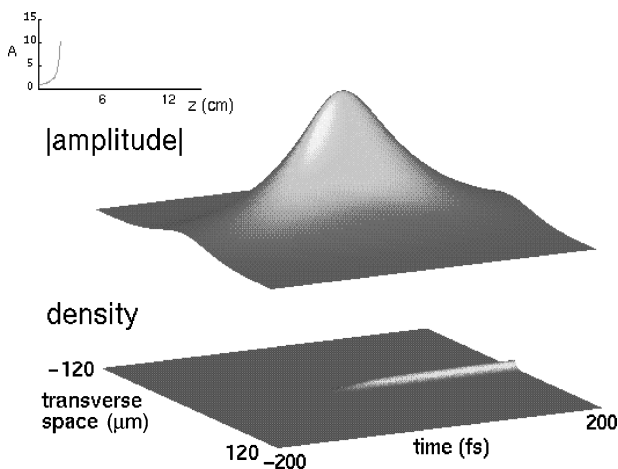

FIG. 10. Space-time (r,t) pulse profile at the propagation distance $z=2.3$ cm, $p=10$ atm, and $P_{in}=1.975P_{cr}$. The inset shows the maximum over time of the electric field amplitude.
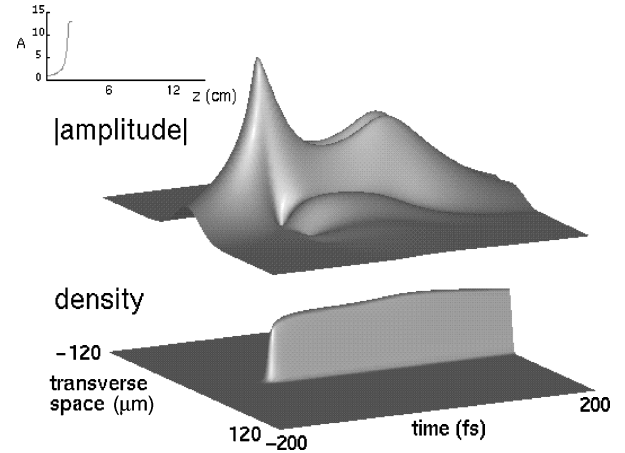
observed this process for femtosecond pulse propagation in air [46] where we term it dynamic spatial replenishment to distinguish it from the progressive pulse splitting process due to GVD [21–26].

For Ar at 10 atm we also observe that there is a range of input powers for which we observe a sustained maximum (over time) of the on-axis intensity over longer propagation distances (on the order of centimeters). An example of this prolonged propagation is shown in Fig. 12(a) and shows that after the SF collapse is arrested by MPI it maintains itself at a distance of around 10 cm. Closer examination reveals that it is the second subpulse that produces the prolonged propagation after the leading edge pulse has decayed.

Recently, in Ref. [47] it was suggested that such prolonged propagation in a focusing geometry can be due to self-trapping stabilized by plasma-defocusing. Figure 12(b) shows the corresponding electron density in our computations and we see that beyond $z=3$ cm plasma generation leading to absorption of the field is not significant. This suggests a mechanism other than plasma defocusing is responsible for the stabilization.
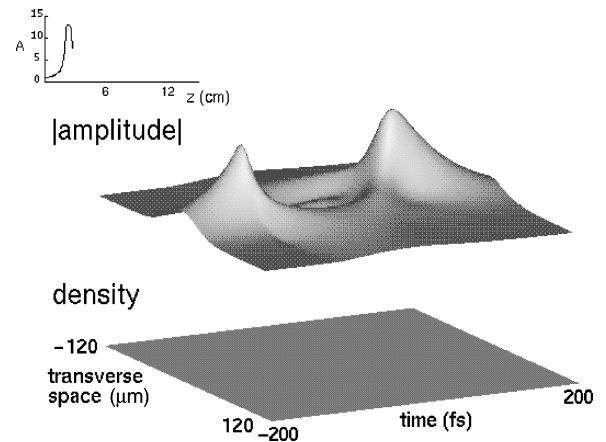

FIG. 9. Space-time (r,t) pulse profile at the propagation distance $z=2.0$ cm, $p=10$ atm, and $P_{in}=1.975P_{cr}$. The inset shows the maximum over time of the electric field amplitude.

FIG. 11. Full (r,t)-space electric field amplitude plot and the corresponding density of the generated plasma at the propagation distance $z=2.7$ cm at 10 atm. The input power is $P=1.975P_{cr}$. The inset shows the maximum over time of the electric field amplitude.
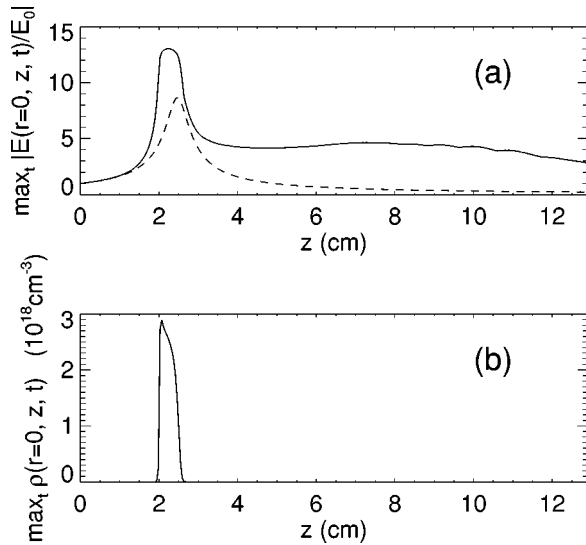
FIG. 12. (a) Maximum over time of the on-axis electric field amplitude and (b) on-axis density of generated plasma at 10 atm. $P = 1.975 P_{cr}$. [The dashed line in (a) denotes the behavior of the maximum on-axis field amplitude over time for linear propagation.]
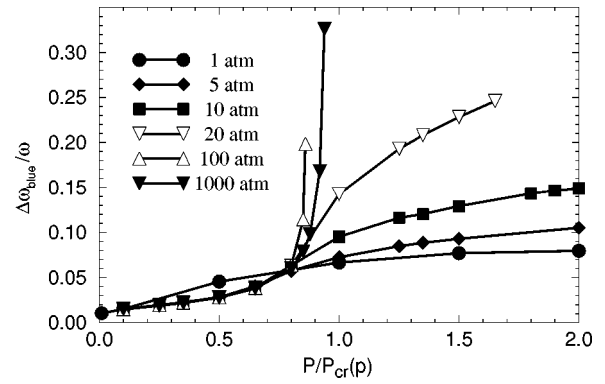

FIG. 13. Blue-side superbroadening/plasma broadening of the pulse spectrum as a function of the input power. The procedure of extracting this information from the data is described in the text.

We attribute this prolonged propagation to self-channeling produced by the combined effects of SF and (weak) GVD, which can lead to the existence of the long-range pulse propagation beyond the linear focus. It is well known that self-trapping is unstable in two dimensions [14], but GVD can produce some stabilization through pulse splitting as mentioned previously. During this process a conical emission is observed numerically [48], which could explain the experimental observations. Having said this, we remark that this stabilization is somewhat fragile and is already lost for a peak input power $P_{in} \gtrsim 1.98 P_{cr}$, for which the second pulse continues to self-focus rather than stabilize. Also, as the pulse propagates it undergoes temporal compression due to SF [49,50] and eventually splits. This can lead to pulse lengths on the order of 10 fs, where one has to be careful about interpreting the results of our model, which assumes a slowly varying envelope approximation. At this stage one should consider adding other correction terms consistently to the model (shock terms, etc.) or transition to a full Maxwell equation description.

D. Blue-side superbroadening of the pulse spectrum

If we constrain ourselves to the region of parameters for which we believe our slowly varying envelope and paraxial approximation are valid, we can actually compare our results with the experimental characteristics. In this paper we choose as a characteristic the blue-side superbroadening of the spectrum, that is, the spectral width of the transmitted pulse on the blue side normalized to the pulse center frequency, and compare it to the measured counterpart in gaseous CO_2 at a pressure of 35 atm [17].

In Fig. 13 we plot the width of the spectral region between the central frequency of the pulse and the frequency (on the blue side) at which the spectral intensity reaches 10^{-6} of its value at maximum for different Ar pressures as a function of input pulse power P_{in}. Notice that the input power of the pulse is normalized to the respective critical power P_{cr}, which is pressure dependent (n_b and mainly n_2 are pressure dependent). For low pressures we see that the blue-side broadening increases with increasing input power, due to plasma-induced blueshifting, but does not show any particular features as the input power approaches the critical power, indicating the SF is not relevant in the low-pressure regime [7,8]. In contrast, for higher pressures $p > 100$ atm the blue-side broadening increases dramatically as the critical power is approached, indicative of both strong SF and associated superbroadening [16].

Our results for the blue-side broadening may be compared with the experimental results in Fig. 5 of Francois *et al.* [17] using CO_2 at 35 atm. We find qualitative agreement in that there is a dramatic increase in the blue-side broadening as the critical power is approached for pressures $p \gtrsim 20$ atm (supercontinuum threshold). After reaching the threshold for breakdown the broadening slows down but does not reach a constant value (see Fig. 13).

IV. SUMMARY AND CONCLUSIONS

In summary, we have developed a comprehensive model for nonlinear pulse propagation in gaseous media, which solves the NLSE coupled to a rate equation describing plasma generation. The model has been used to perform numerical simulations of nonlinear propagation in Ar, using visible pulses of 200-fs duration and in a focusing geometry.

Our primary goal in this study was to examine how plasma effects and self-focusing interact during ultrashort pulse propagation in Ar at different pressures and point out the limiting cases that were studied previously and the problems one has to deal with in different pressure regimes. To this end we used a model incorporating the effects of plasma-pulse interaction, self-focusing, multiphoton absorption, and group velocity dispersion.

We found the most interesting features of femtosecond pulse propagation in the intermediate region of pressures, where both the Kerr nonlinearity and plasma effect play a significant role. In the presence of the plasma the pulses with sufficient power undergo self-focusing until their intensity is high enough to generate the plasma via MPI initially. The initial electron density can also serve as a seed of the avalanche ionization in the trailing portion of the pulse. A dy-

namic picture of multiple subpulse creation emerges that differs from that of pulse splitting due to GVD. The trailing part of the pulse is spatially defocused by the plasma and, if it has enough power, can actually refocus again. This replenishment mechanism creates a subpulse, which can either diffract or self-focus again and propagate beyond the linear focus due to the combined effect of self-focusing and (normal) group velocity dispersion. We showed qualitative agreement of the blue-side spectral broadening of the pulses as a function of the input power for different pressures with the experimental results.

[1] A. L. A. E. Huillier, L. A. Lompre, G. Mainfray, and C. Manus, Phys. Rev. A **27**, 2503 (1983).

[2] T. S. Luk, H. Pummer, K. Boyer, M. Shahidi, H. Egger, and C. K. Rhodes, Phys. Rev. Lett. **51**, 110 (1983).

[3] M. D. Perry, O. L. Landen, A. Szöke, and E. M. Campbell, Phys. Rev. A **37**, 747 (1988).

[4] W. M. Wood, G. Focht, and M. C. Downer, Opt. Lett. **13**, 984 (1988).

[5] M. C. Downer, Wm. M. Wood, and J. I. Trisnadi, Phys. Rev. Lett. **65**, 2832 (1990).

[6] Wm. M. Wood, C. W. Siders, and M. C. Downer, Phys. Rev. Lett. **67**, 3523 (19910).

[7] S. C. Rae and K. Burnett, Phys. Rev. A **46**, 1084 (1992).

[8] S. P. LeBlanc, R. Sauerbrey, S. C. Rae, and K. Burnett, J. Opt. Soc. Am. B **10**, 1801 (1993).

[9] R. Rankin, C. E. Capjack, N. H. Burnett, and P. B. Corkum, Opt. Lett. **16**, 835 (1988).

[10] S. C. Rae, Opt. Commun. **97**, 25 (1993).

[11] C. G. Durfee III and H. M. Milchberg, Phys. Rev. Lett. **71**, 2409 (1993).

[12] P. L. Kelley, Phys. Rev. Lett. **15**, 1005 (1965).

[13] V. E. Zakharov, V. V. Sobolev, and V. C. Synakh, Zh. Eksp. Teor. Fiz. **60**, 136 (1971) [Sov. Phys. JETP **33**, 77 (1971)].

[14] J. H. Marburger, Prog. Quantum Electron. **4**, 35 (1975).

[15] N. Bloembergen, Opt. Commun. **8**, 285 (1973).

[16] P. B. Corkum, C. Rolland, and T. Srinivasan-Rao, Phys. Rev. Lett. **57**, 2268 (1986).

[17] V. Francois, F. A. Ilkov, and S. L. Chin, J. Phys. B **25**, 2709 (1992).

[18] F. A. Ilkov, L. Sh. Ilkova, and S. L. Chin, Opt. Lett. **18**, 681 (1993).

[19] D. Strickland and P. B. Corkum, Proc. SPIE **1413**, 54 (1991).

[20] D. Strickland and P. B. Corkum, J. Opt. Soc. Am. B **11**, 492 (1994).

[21] N. A. Zharova, A. G. Litvak, T. A. Petrova, A. M. Sergeev, and A. D. Yunakovskii, Pis'ma Zh. Eksp. Teor. Fiz. **44**, 12 (1986) [JETP Lett. **44**, 13 (1986)].

[22] P. Chernev and V. Petrov, Opt. Lett. **17**, 172 (1992).

[23] J. E. Rothenberg, Opt. Lett. **17**, 583 (1992).

[24] G. G. Luther, J. V. Moloney, A. C. Newell, and E. M. Wright, Opt. Lett. **19**, 862 (1994).

[25] J. K. Ranka, R. W. Schirmer, and A. L. Gaeta, Phys. Rev. Lett. **77**, 3783 (1996).

[26] L. Berge *et al.*, J. Opt. Soc. Am. B **13**, 1879 (1996); Phys. Plasmas **3**, 824 (1996); Phys. Rev. E **53**, R1340 (1996).

[27] M. D. Feit and J. A. Fleck, Appl. Phys. Lett. **24**, 169 (1974).

[28] Q. Feng, J. V. Moloney, A. C. Newell, E. M. Wright, K. Cook, P. K. Kennedy, D. X. Hammer, and C. R. Thompson, IEEE J. Quantum Electron. **33**, 127 (1997).

[29] L. V. Keldysh, Sov. Phys. JETP **20**, 1307 (1965).

[30] R. R. Freeman, P. H. Bucksbaum, H. Milchberg, S. Darack, D. Schumacher, and M. E. Geusic, Phys. Rev. Lett. **59**, 1092 (1987).

[31] E. Yablonovitch and N. Bloembergen, Phys. Rev. Lett. **29**, 907 (1972).

[32] E. R. Peck and J. D. Fisher, J. Opt. Soc. Am. **54**, 1362 (1964).

[33] Y. Shimoji, A. T. Fay, R. S. F. Chang, and N. Djeu, J. Opt. Soc. Am. B **6**, 1994 (1989).

[34] P. Sitz and R. Yaris, J. Chem. Phys. **49**, 3546 (1968).

[35] V. Mizrahi and D. P. Shelton, Phys. Rev. Lett. **55**, 696 (1985).

[36] The $\beta^{(8)}$ actually calculated using the data in [3].

[37] Yu. P. Raizer, *Plasma Physics* (Springer, Berlin, 1994).

[38] S. N. Vlasov, L. V. Piskunova, and V. I. Talanov, Zh. Eksp. Teor. Fiz. **95**, 1945 (1989) [Sov. Phys. JETP **68**, 1125 (1989)].

[39] G. Strang, SIAM (Soc. Ind. Appl. Math.) J. Numer. Anal. **5**, 506 (1968).

[40] G. R. Hadley, Opt. Lett. **16**, 624 (1991).

[41] J.E. Rothenberg, Opt. Lett. **17**, 1340 (1992).

[42] T. Brabec and F. Kraus, Phys. Rev. Lett. **78**, 3282 (1997).

[43] G. Fibich and G. C. Papanicolaou, Opt. Lett. **22**, 1379 (1997).

[44] E. Yablonovitch, Phys. Rev. A **10**, 1888 (1974).

[45] A. Sergeev, E. Vanin, L. Stenflo, D. Anderson, M. Lisak, and M. L. Quiroga-Teixeiro, Phys. Rev. A **46**, 7830 (1992).

[46] M. Mlejnek, E. M. Wright, and J. V. Moloney, Opt. Lett. **23**, 382 (1998).

[47] H. R. Lange, G. Grillon, J.-F. Ripoche, M. A. Franco, B. Lamouroux, B. S. Prade, and A. Mysyrowicz, Opt. Lett. **23**, 120 (1998).

[48] G. G. Luther, A. C. Newell, J.V. Moloney, and E. M. Wright, Opt. Lett. **19**, 789 (1994).

[49] J. H. Marburger and W. G. Wagner, IEEE J. Quantum Electron. **3**, 415 (1967).

[50] G. L. McAllister, J. H. Marburger, and L. G. DeShazer, Phys. Rev. Lett. **21**, 1648 (1968).